

Quantum Conductors Formation and Resistive Switching Memory Effects in Zirconia Nanotubes

A.S. Vokhmintsev¹, I.A. Petrenyov¹, R.V. Kamalov¹, I.A. Weinstein^{1,2*}

¹ NANOTECH Center, Ural Federal University, Ekaterinburg, 620002, Russia
² Institute of Metallurgy of the Ural Branch of the Russian Academy of Sciences, Ekaterinburg 620016, Russia

*e-mail: i.a.weinstein@urfu.ru

Abstract

The development prospects of memristive elements for non-volatile memory with use of the metal-dielectric-metal sandwich structures with a thin oxide layer are due to the possibility of reliable forming the sustained functional states with quantized resistance. In the paper we study the properties of fabricated memristors based on the non-stoichiometric ZrO₂ nanotubes in different resistive switching modes. Anodic oxidation of the Zr foil has been used to synthesize a ZrO₂ layer of 1.7 μm thickness, consisting of an ordered array of vertically oriented nanotubes with outer diameter of 75 nm. Zr/ZrO₂/Au sandwich structures have been fabricated by mask magnetron deposition. The effects of resistive switching in the Zr/ZrO₂/Au memristors in unipolar and bipolar modes have been investigated. The resistance ratios $\geq 3 \cdot 10^4$ between high-resistance (*HRS*) and low-resistance (*LRS*) states have been evaluated. It has been founded the conductivity of *LRS* is quantized in a wide range with minimum value of $0.5G_0 \approx 38.74 \mu S$ due to the formation of quantum conductors based on oxygen vacancies (V_O). Resistive switching mechanisms of Zr/ZrO₂/Au memristors with allowing for migration of V_O in an applied electric field have been proposed. It has been shown that the ohmic type and space charge limited conductivities are realized in the *LRS* and *HRS*, correspondingly. We present the results which can be used for development of effective memristors based on functional Zr/ZrO₂/Au nanolayered structure with multiple resistive states and high resistance ratio.

Keywords

ZrO₂, memristor, quantum conductive filaments, resistance state, oxygen vacancies

Introduction

Today zirconium dioxide is being actively used in various high-tech fields such as the generation and storage of electrical energy [1, 2, 3], optical and laser technology [4], catalysis [5, 6, 7], photonics [8], solid-state dosimetry of ionizing radiation [9,10], nanoelectronics [11,12,13], biomedicine [3, 14, 15,], etc. The prospect of creating memristor elements of non-volatile memory based on metal-dielectric-metal (MDM) sandwich structures with a ZrO₂ layer is due to their outstanding properties. Among the latter are low energy consumption [16, 17, 18, 19, 20], high on/off current ratio [19, 20, 21, 22, 23, 24], high-speed performance [16, 18, 19, 20, 24, 25, 26, 27, 28] and meantime-to-failure (endurance), a variety of morphology and methods of manufacturing the active layer, the possibility of scaling [17, 18, 24, 28] and creating three-dimensional integrated circuits [21, 29], applications in flexible electronics [21], as well as compatibility with the existing CMOS technology [16, 30].

It is known that the resistive switching in the oxide layer of MDM structures underlying the memory device operation is usually provided by the mobility of anionic (V_O) vacancies [20, 25, 27, 28,29, 31, 32, 33], ions of impurity metals [18, 19, 20, 24, 26, 33, 34, 35] or Zr⁺ [16, 28, 36] in the active layer under an external electric field. The electrical resistance of the memristor in low-resistance (*LRS*), high-resistance (*HRS*) and intermediate states are governed by the thickness and imperfection of the dioxide layer [23, 24, 28, 31, 32, 37]. In this case, one of the most probable

mechanisms of resistive switching in as-grown ZrO₂-based structures is the chain-ordering of V_O vacancies followed by the formation of conductive channels or filaments between metal contacts. Subsequently, in applying a control voltage U , the conductive filaments (CF) are partially destroyed and/or restored. Thus, a reversible switching of the memristor between the corresponding resistive states ($LRS \leftrightarrow HRS$) in both unipolar [22] and bipolar [36] modes is realized.

There are various methods for improving the characteristics of memristors based on functionalized ZrO₂ layers. To improve the stability and operational lifetime of memristor structures, in this context, the selection of materials for electrodes [21, 17, 25], the creation of nanocomposites with organic compounds [34], and combinations of several oxide layers [23] should be worth mentioning. Conductive metal filaments made of materials embedded in the active layer at the stage of electroforming the memristors can be provided by ion implantation [36, 26] and incorporation of metal nanocrystals into the oxide [24]. A rise in the degree of dioxide non-stoichiometry in oxygen makes it easier for further electroformation of Zr [16] or V_O [22] filaments in the active layer.

An oxygen deficiency increase in various oxide structures during their synthesis can be achieved by the method of electrochemical oxidation through fitting conditions and anodizing parameters [21, 38, 39, 40, 41, 42]. In particular, it was shown in [38, 43, 44, 45, 46, 47, 48] that MDM structures based on nanotubular layers of non-stoichiometric TiO_{2-x}, obtained by the anodization technique, are breakthrough materials as memristor memory cells.

To date, only one scientific group has examined the effects of resistive switching in 40 nm thick ZrO₂ layers produced by the method of anodic oxidation at room temperature in the galvanostatic mode in an aqueous solution of phosphoric acid [21, 49]. Earlier, we have reported the results of studies of the current-voltage characteristics of nanotubular ZrO₂ layer-based as-grown MDM structures with unidirectional conductivity, obtained by the anodic oxidation method [37, 32] in the potentiostatic mode. The present paper is aimed at measuring and analyzing the static current-voltage (I - V) characteristics of fabricated nanoelectronic devices based on a ZrO₂ nanotubular layer in unipolar and bipolar resistive switching modes, and also at describing the peculiarities of electroformation of memristors and the latter's switching mechanisms.

Experimental

Synthesis of a Nanotubular ZrO₂ Layer

A layer of nanotubular zirconium dioxide (ZrO₂-nt) was fabricated by two-stage anodic oxidation of a Zr substrate containing Hf < 4% in a two-electrode cell at a constant voltage of 20 V. A 100 μm-thick Zr foil was preliminarily degreased with acetone, treated with an acid solution in the ratio HF:HNO₃:H₂O = 1:6:20, washed with distilled water and dried in air. The electrolyte was a solution of ethylene glycol containing 5 wt.% H₂O and 1 wt.% NH₄F [42]. During anodization, the anode and electrolyte were maintained at constant temperatures of 10 and 20 °C, respectively. The duration of the primary and secondary anodizing amounted to 5 min. After primary anodization, the obtained oxide layer was etched with the above acid solution.

Creating Zr/ZrO₂-nt/Au Sandwich Structures

50 nm-thick Au contacts were deposited onto the as-grown ZrO₂-nt layer by magnetron sputtering of gold through a mask mounted on a combined system Q150T ES, Quorum Technologies. Within the sequence-linked operations of the technological cycle specified, more than 100 independent Zr/ZrO₂-nt/Au sandwich structures were produced in such a way.

Characterization of Zr/ZrO₂-nt /Au Sandwich Structures

The morphology of the as-grown oxide layer was analyzed using a SIGMA VP scanning electron microscope (SEM), Carl Zeiss. The obtained SEM images were processed by a SIAMS 800 automatic system. Imaging the fabricated sandwich structures was carried out using an Axio CSM

700 confocal optical microscope, Carl Zeiss. Built-in standard tools of the Axio CSM 700 Software program provided analyzing the pictures. Figure 1a shows an optical microscope image for a series of memristor structures under study. It can be inferred that all the fabricated memristors have a diameter of $140 \pm 5 \mu\text{m}$ and surface roughness parameters such as arithmetical mean deviation of the assessed profile $R_a = 250 \text{ nm}$ and root mean squared $R_q = 350 \text{ nm}$.

Structural characterization of as-grown oxide layer was performed by Rigaku Min-iFlex 600 diffractometer with a copper anode using the Rietveld method. The scanning speed was $0.3^\circ/\text{min}$ with step of 0.02° . The diffraction data analysis was carried out in the SmartLab Studio II software.

Recording Current-Voltage Characteristics

The measurements of I - V characteristics of the fabricated $\text{Zr}/\text{ZrO}_2\text{-nt}/\text{Au}$ memristors were taken using a PXIe-4143 NI modular controlled power supply unit and a Cascade Microtech MPS 150 microprobe station [50]. The Zr substrate was grounded, and the harmonic voltage $U(t)$ with a frequency of 0.01 Hz and amplitude $U_{max} = 4 \text{ V}$ was applied to the Au contact (see Figure 1b).

Before measuring the I - V curves, each as-grown memristor was subjected to electroformation (EF). This procedure was implemented by applying a positive or negative polarity voltage $U(t)$ that harmonically varied from 0 to U_{max} . The current flowing through the structure was limited to $\pm 0.1 \text{ mA}$ (see Figure 1c,d, EF line). Once the EF procedure finished, the memristors saved LRS . The subsequently resistive switching was carried out both in bipolar and unipolar modes.

In bipolar mode, a positive polarity signal of $U(t)$ first switched the memristors from LRS to HRS ($LRS \rightarrow HRS$), which corresponded to the “Reset” operation. Then, a negative polarity signal of $U(t)$ returned them in the initial state ($HRS \rightarrow LRS$). Such an operation was identified as the “Set” one (see Figure 1c).

In unipolar mode, only a positive polarity voltage $U(t)$ brought about switching the memristors. First, the “Reset” operation and then the “Set” operation were implemented (see Figure 1d). The “Reset” and “Set” operations successively performed comprise one complete cycle of the resistive switching of the memristor. Figure 1e sketches a flowchart of the I - V recording process. Thus, the I - V curves of the fabricated memristors were recorded over 20 full cycles of both resistive switching modes. The electrical resistance of the memristors in LRS (R_{LRS}) and HRS (R_{HRS}) was determined from the experimental dependencies of the current passing through the memristor on the applied voltage of $U = \pm 0.5 \text{ V}$, $I(U)$.

So, a schematic representation of the $\text{Zr}/\text{ZrO}_2\text{-nt}/\text{Au}$ memristor with connected electrical contacts and the order of the I - V curve measurements are shown in Figure 1b – e.

Electric Capacity Measurement

The electric capacity of the memristors at hand was measured after switching $LRS \rightarrow HRS$. For this, a NI PXI-4072 modular digital multimeter and a Cascade Microtech MPS 150 microprobe station were used.

Results

Structural Characterization

Figure 2a contains SEM images of a synthesized nanotubular $\text{ZrO}_2\text{-nt}$ layer. In the presented image, the oxide layer has a thickness of $\approx 1.7 \mu\text{m}$ and consists of nanotubes vertically oriented to the substrate. The nanotubes are open on one side (Figure 2b), and closed on the side of the Zr-substrate (Figure 2c).

Figure 2d displays a histogram and a curve of the normal internal-diameter-distribution (solid black line in the Figure) for a series of 10^3 nanotubes. Analyzing the obtained images showed that the synthesized oxide layer consists of an ordered array of nanotubes whose average values of inner and external diameters are (55 ± 7) and (75 ± 10) nm, respectively. The average wall thickness of nanotubes amounts to (10 ± 5) nm.

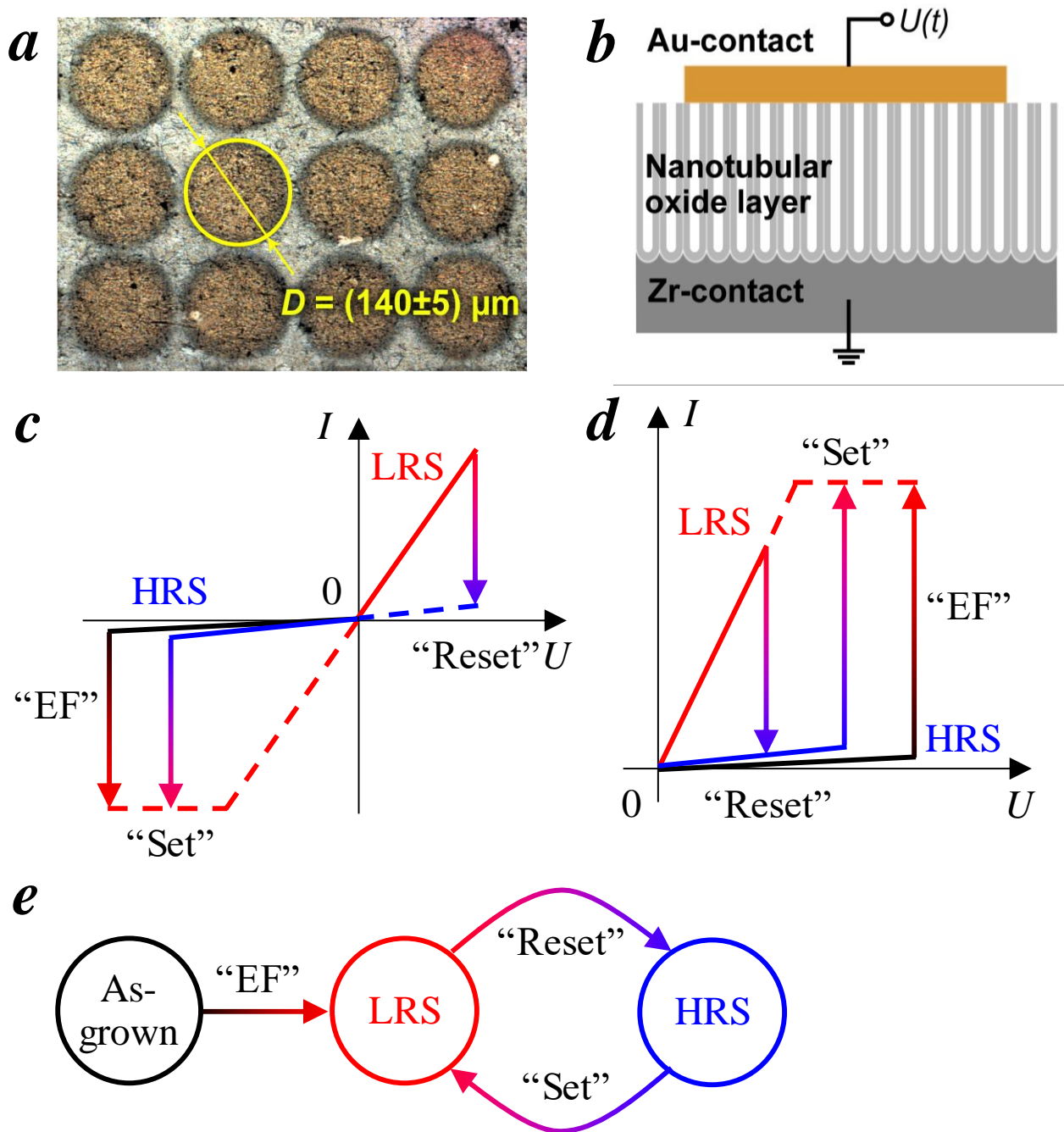


Figure 1. Images of fabricated Zr/ZrO₂-nt/Au memristors and the I - V measurement sequence. (a) Optical image of Au contacts on the surface of the oxide layer. (b) Schematic representation of the structure of a single memristor with connected electrical contacts. (c, d) Schematic I - V curves of memristors operating in bipolar and unipolar switching modes, respectively. (e) The sequence of changes in the resistive states of memristors.

Figure 3 shows the XRD pattern of ZrO₂-nt layer. When the background signal (see Fig. 3, dash line) is taken into account, it can be seen that there are a halo (Fig. 3, gray filling) and two broad peaks with maxima near $2\theta = 30$ and 50° (Fig. 3, violet filling) on the experimental curve. The halo is due to the amorphous phase, the peaks are related to the crystal structure of the ZrO₂-nt sample. The observed peaks can be presented by reflexes superposition from tetragonal (t) (scattering angles $2\theta = 30.86, 34.32, 36.49, 43.29, 50.96, 52.57, 59.32, 62.21, 64.30, 72.33, 77.54, 78.14, 83.22^\circ$, see Fig. 3, green pattern) and monoclinic (m) (at $2\theta = 18.41, 25.47, 27.54, 35.25, 35.326, 37.32, 39.81, 49.94, 50.94, 52.32, 53.80, 55.55, 57.35, 57.67, 61.67, 65.97, 70.29^\circ$, see Fig.

3, red pattern) phases. Using standard analysis, it was evaluated that the nanotubes composition is characterized by mixture of t- (43%), m- (32%) and a-ZrO₂ (25%) phases.

It is well known that for bulk zirconia the phase transition of the monoclinic structure to the tetragonal one takes place at 1170 °C [51]. However, the data obtained are in satisfactory agreement with studies of phase transformations in the low-temperature sintering process (200 – 350 °C) during the crystallization of an amorphous ZrO₂ nanopowder performed by decomposition of zirconium carbonate [52]. The crystallization [52] proceeds with the formation of predominantly t-phase with 36 ± 6 nm grain size and the appearing of m-ZrO₂ (15 – 20 %). In our case, the dominance of the tetragonal symmetry may exhibit the presence of structural features < 30 nm – for example, the wall thickness of the synthesized zirconia nanotubes is near 10 nm, see *Structural Characterization section*.

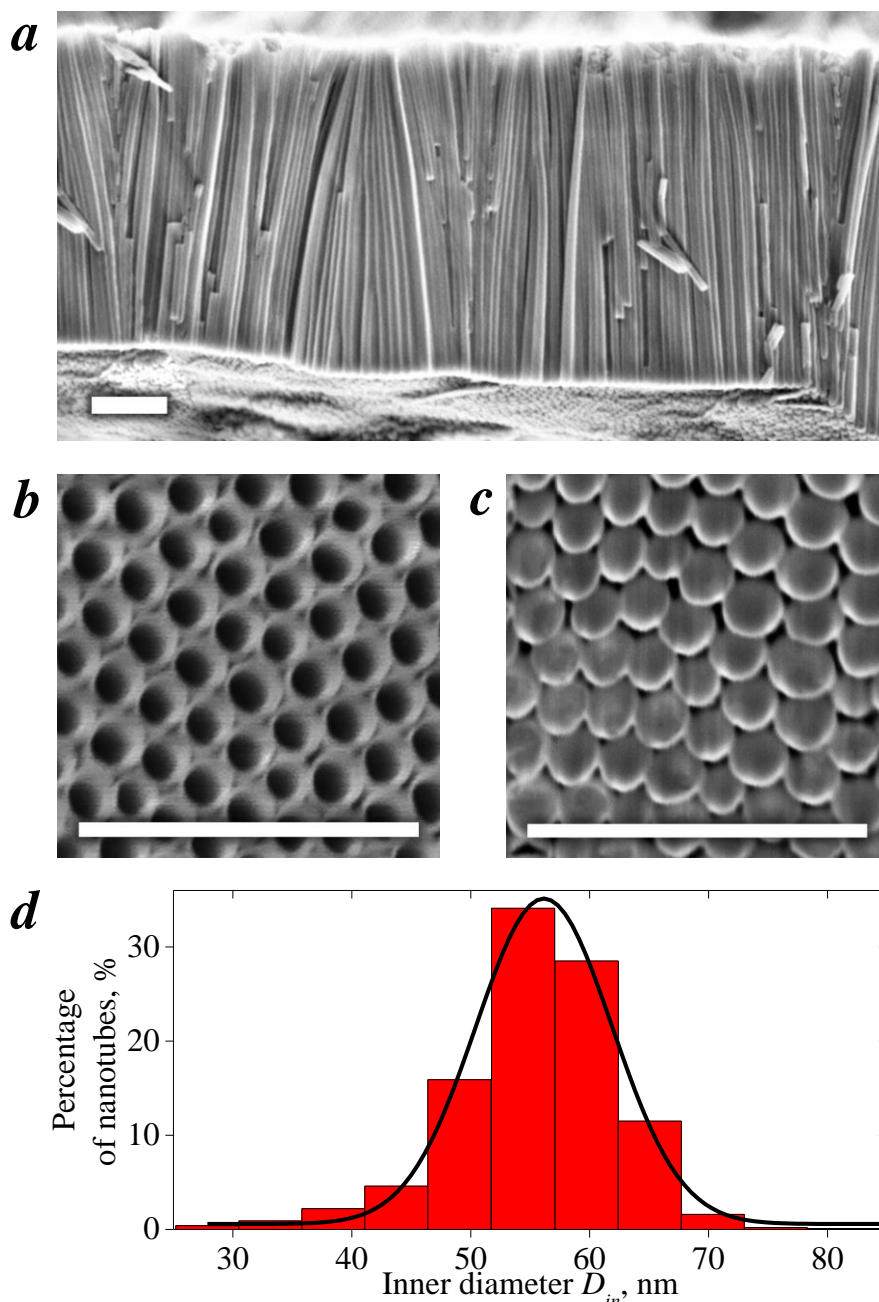


Figure 2. SEM characterization of an anodized ZrO₂-nt layer. (a – c) Cross-section, top view (from the side of Au contacts deposited) and bottom view (from the side of the Zr substrate) of the synthesized oxide layer, respectively. (d) A histogram of the internal-diameter distribution of nanotubes. The black solid line is a normal distribution.

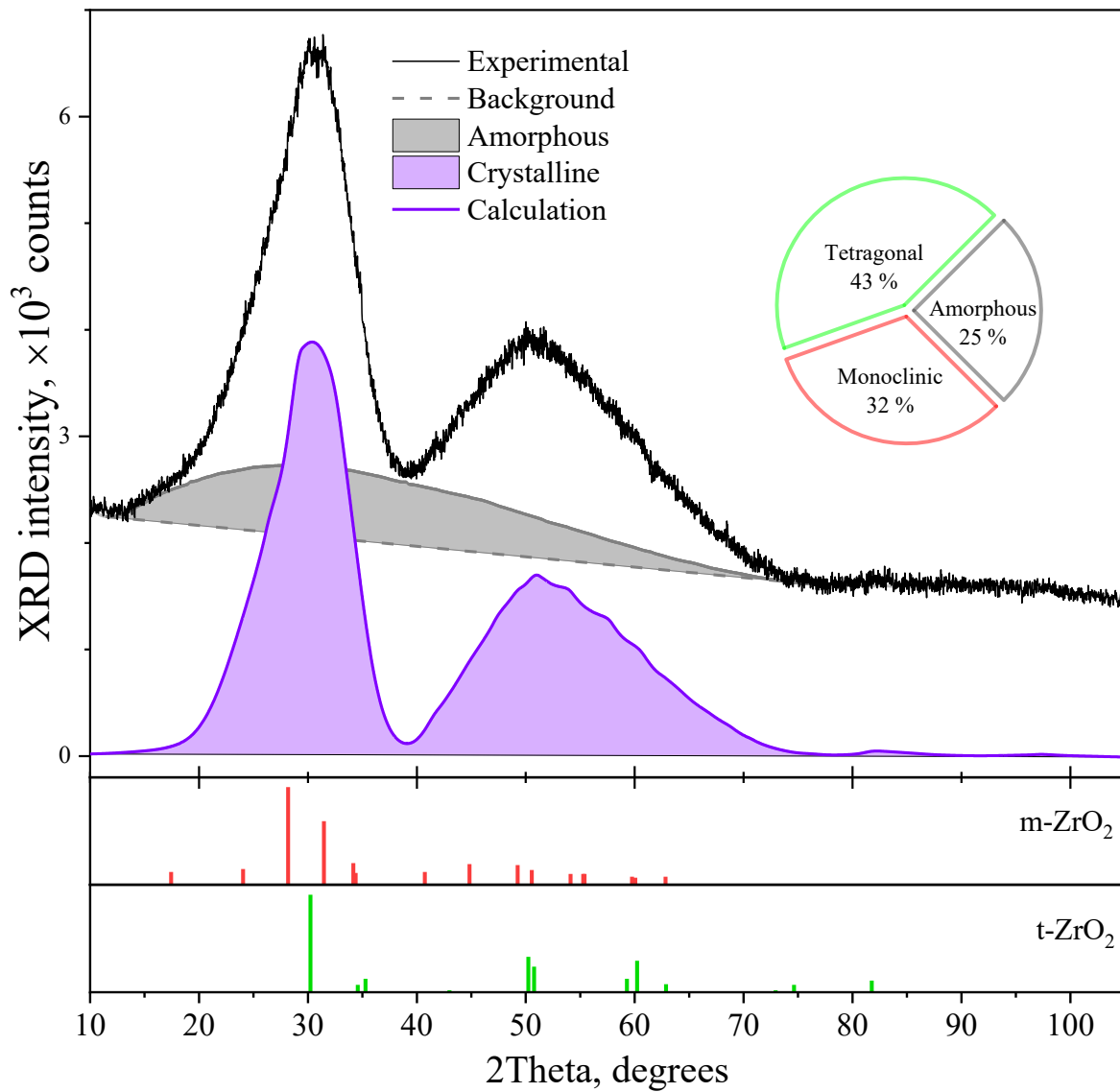


Figure 3. XRD patterns and phase composition analysis for synthesized $\text{ZrO}_2\text{-nt}$ layer.

Current-Voltage Characteristics

Figures 4a, b presents the experimental I - V curves of the memristors investigated for 20 cycles of bipolar and unipolar switching, respectively. Vertical arrows indicate the instants of a sharp change in current through memristors due to the transition of the structure between resistive states ("Reset" and "Set" operations). Some I - V characteristics contain short-term surges and jumps. This can be explained by a change in the electrical resistance of the structure when U slightly increases. It is clear from the EF curves that the as-grown $\text{Zr}/\text{ZrO}_2\text{-nt}/\text{Au}$ structure exhibits characteristics close to those being in *HRS*. A further increase in applied voltage leads to the primary formation of CFs at $U_{EF} \approx -2.4$ and 4V for bipolar and unipolar switching modes, respectively. Subsequently, the "Reset" operation is realized at voltages of $U_{RES} = 0.6 \pm 0.1$ and 1 ± 0.1 V, and the "Set" operation takes place at voltages of $U_{SET} = -2 \pm 0.3$ and 3.5 ± 0.5 V for bipolar and unipolar modes, respectively.

Thus, the formation of CFs in the oxide layer shunts the Schottky barrier at the Au/ZrO_2 interface [25, 35] and eliminates the unidirectional conductivity effect in the as-grown $\text{Zr}/\text{ZrO}_2\text{-nt}/\text{Au}$ structure [42].

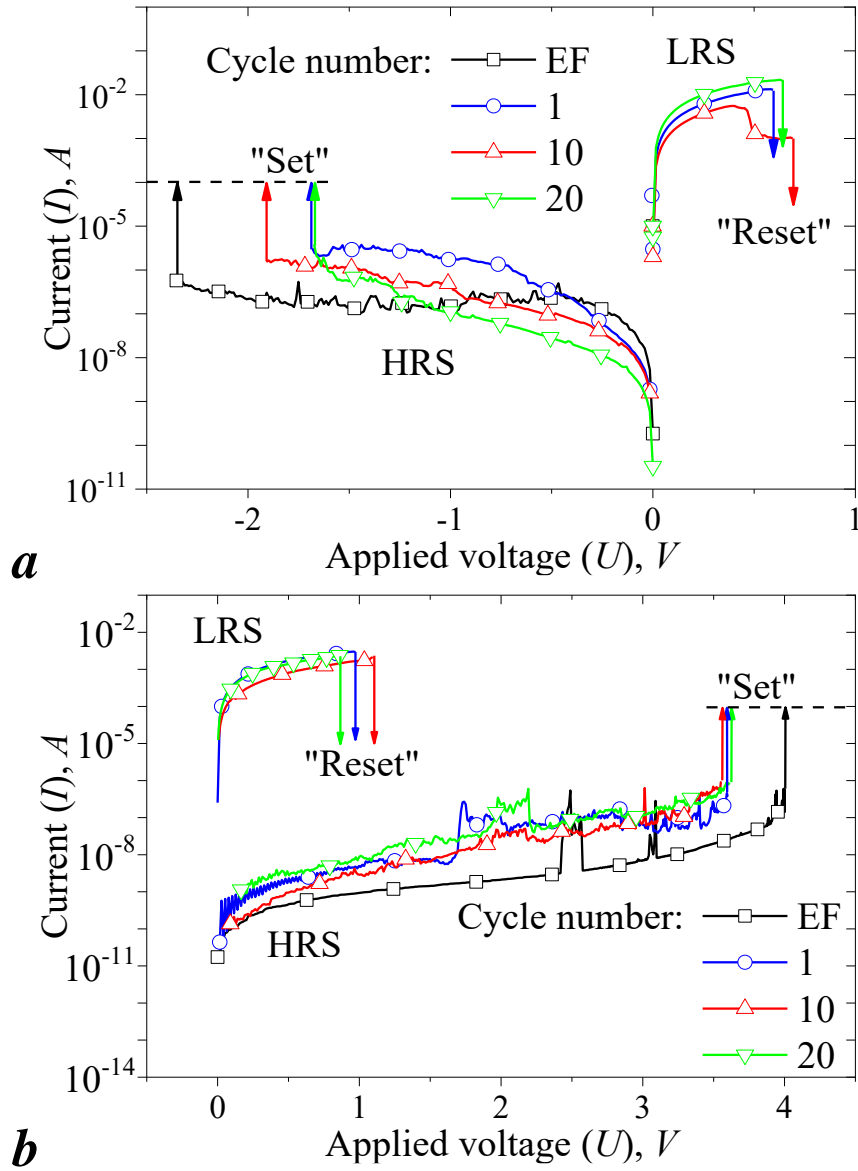


Figure 4. Current-voltage characteristics of Zr/ZrO₂-nt/Au memristors in (a) bipolar and (b) unipolar resistive switching modes, respectively. Vertical arrows indicate a change in the resistive state of the memristors. Dotted lines denote the limitation level of current passing through the memristors during their HRS → LRS switching. EF is electroforming curves. Digits are numbers of complete measurement cycles.

Discussion

For discussing the findings secured, all the experimental I - V characteristics (see Figure 4) were plotted in the following coordinates: surface current density J depending on an electric field E , with the oxide layer thickness $d = 1.7 \mu\text{m}$ and memristor's Au contact area $S = 1.5 \times 10^4 \mu\text{m}^2$ taking into account. An analysis of the $J(E)$ curves accounts for the geometric dimensions of the memristor structures and compares their resistive switching characteristics with those in other papers. Table 1 summarizes the switching mode parameters and morphological features of the Zr/ZrO₂-nt/Au structure in comparison with independent data for memristors based on amorphous [22, 23, 24, 26, 36], polycrystalline [16, 17, 20, 29, 31, 33, 53] and nanocomposite [34] ZrO₂ layers.

Analysis of C-V Curves

Figures 5a, b illustrates changes in the values of the electric field strength (E_{SET} and E_{RES}) and resistance (R_{LRS} and R_{HRS}) for 20 complete cycles of resistive switching of the memristors in bipolar

and unipolar modes, respectively. The experimental values of E for the switching memristors are in the ranges $E_{SET} = -10 - -14$ and $17 - 23$ kV/cm and $E_{RES} = 2.9 - 4.1$ and $5.4 - 6.4$ kV/cm for bipolar and unipolar modes, respectively. It should be emphasized that $E_{SET} \approx (3 - 4) E_{RES}$ for both switching modes of the memristors tested. At the same time, the scatter of the E_{SET} and E_{RES} values for the memristors may take place because of the variation of the ZrO_2 -nt layer thickness within $1.7 \pm 0.1 \mu m$ and the uncontrolled creation of a multitude of conductive filaments during electroforming.

From Table 1, it is seen that the primary formation of filaments and further resistive switching in the synthesized Zr/ZrO_2 -nt/Au is realized at lower E values despite a thicker oxide layer compared to the memristor structures presented. This appears to be caused by several factors, for example, firstly, due to a high concentration of oxygen vacancies in the anodized ZrO_2 . So in [54], the X-ray photoelectron spectroscopy method demonstrates a high photocatalytic activity of oxygen vacancies in nanotubular ZrO_{2-x} obtained by the anodization method.

Secondly, the oxide layer of the memristors has the nanotubular morphology. Simulating the distribution of the electric field strength throughout the nanotubular structure confirms the emergence of increased strength regions in the base of the nanotubes, which determines their growth during anodization (see the example of TiO_2 in [55]). Besides, the influence of surface roughness of the Au/ TiO_2 interface for memristor structures based on a 20 nm thick TiO_2 film synthesized by magnetron sputtering was explored in [56]. The authors showed that the values of memristor resistive switching voltages diminish with increasing the roughness in the range of $Rq = 4.2 - 13.1$ nm. This is due to the fact that the sharp roughness peaks heighten the electric field strength. In this case, the formation of CFs occurs in the active layer at lower voltages [56]. Note that in our case, the value of the Rq roughness parameter is noticeably larger (see Section Results. Structural characterization). Thus, the electric and physical characteristics of memristor structures can be improved by the synthesis of thinner nanotubular oxide layers.

Thirdly, the content of Hf impurities in the active layer also can be among the aforementioned factors. This is confirmed by the results of the performed quantitative chemical analysis. Independent data calculated by the density-functional method testifies that the incorporation of isovalent Hf into ZrO_2 contributes to a slight decrease in the V_O -formation energy in the oxide and the improvement of memristor characteristics [27].

It is evident from Figure 5 and Table 1 that the structure resistance in LRS is hundreds of Ω , and tens and hundreds of $M\Omega$ in HRS . It is worth noting that the values of R_{HRS} and R_{LRS} coincide with similar parameters for ZrO_2 -based memristor structures despite the significantly larger thickness of the ZrO_2 -nt layer. There are a lot of papers that contain the fact that the R_{HRS}/R_{LRS} resistance ratios in different states lie in the range of $10 - 10^5$ (see Table 1). In our case, $r = R_{HRS}/R_{LRS} > 37 \cdot 10^4$ and $8 \cdot 10^4$ for unipolar and bipolar switching modes, respectively. The experimental values are comparable with those of the best memristor structures based on thin amorphous ZrO_2 films obtained by electron beam evaporation [22] and subsequent implantation of Zr [36] or Cu [24] ions, see Table 1.

Having compared the obtained parameters of the resistive switching of thin ZrO_2 -layer-based Zr/ZrO_2 -nt/Au structure memristors, the following can be stated: in bipolar mode, lower values of the electric field strength contribute to switching between HRS and LRS . In the process, lower values of r are recorded. The values of the experimentally measured switching parameters of the structures studied allow one to claim that anodized ZrO_2 -based nanotubular layers are promising to use as memristor memory cells.

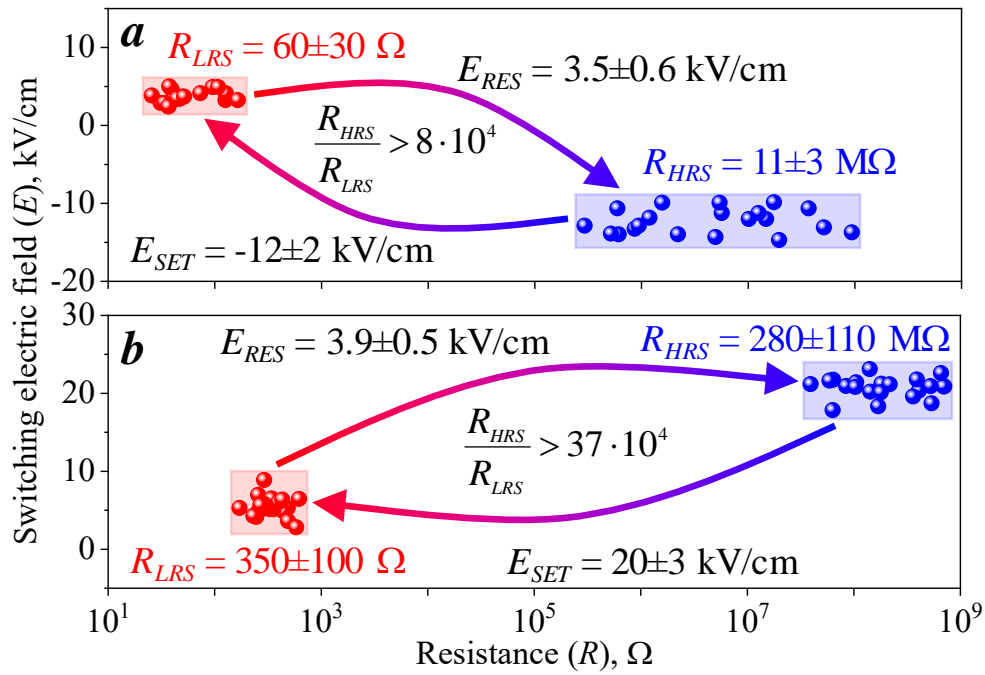


Figure 5. Change in electric field strength (E) and resistance (R) for 20 complete cycles of resistive switching of Zr/ZrO₂-nt/Au memristors for (a) bipolar and (b) unipolar modes. Rectangles indicate the regions of variation of the evaluated characteristics.

Table 1. Switching electric field (E) and electrical resistance (R) values for memristors structures based on the ZrO_2 layers with different morphologies and thickness (d)

No	Mode	Operation, state	E , kV/cm	R , Ω	$r = R_{HRS}/R_{LRS}$	Conduction mechanism and/or behavior	Memristor: structure, size, CFs type	Active layer: thickness, morphology, synthesis technique	Reference		
1	Unipolar	EF, as-grown	23.5	10^9	–	Ohm ^I	Zr/ZrO ₂ -nt/Au, \varnothing 140 μ m ($1.4 \times 10^4 \mu$ m ²), V _O	1.7 \pm 0.1 μ m, nanotubular PC ^{VIII} layer, anodization	This work		
		Set, <i>HRS</i>	-14	$1.7 \cdot 10^7$							
	Reset, <i>LRS</i>	20 \pm 3	$(28 \pm 11) \cdot 10^7$	$> 37 \cdot 10^4$	SCLC ^{II}						
	Set, <i>HRS</i>	5.9 \pm 0.6	350 \pm 100								
Bipolar	Set, <i>HRS</i>	-12 \pm 2	$(11 \pm 3) \cdot 10^6$	$> 8 \cdot 10^4$	SCLC						
	Reset, <i>LRS</i>	3.5 \pm 0.6	60 \pm 30			Ohm					
2	Unipolar	EF	625	No data	–	No data	Zr/ZrO ₂ /Au, \varnothing 500 μ m or 25 \times 25 μ m ²	40 nm, no data, anodization	[21, 49]		
		Set, <i>HRS</i>	225...725	$(5 \dots 260) \cdot 10^4$						$> 10^2$	
		Reset, <i>LRS</i>	75...325	26...130							
3	Unipolar	EF	415–580	No data	–	No data	Pt/ZrO/p ⁺ -Si, 9×10^{-6} cm ² , Zr ⁺	120 nm, PC (t^{IX} and m^{X}) film, magnetron sputtering	[16]		
		Set, <i>HRS</i>	135	$1 \dots 10^4$						> 3	SE ^{III} , Ohm
		Reset, <i>LRS</i>	90								
4	Bipolar	Set, <i>HRS</i>		10^8	$> 3 \cdot 10^4$	SCLC	Au/Cr/ZrO ₂ :Zr ⁺ /n ⁺ -Si, from 50 \times 50 μ m ² to 800 \times 800 μ m ²	70 nm, Zr-implanted amorphous film, EBE ^{IV}	[36]		
		Reset, <i>LRS</i>	\pm 430	$3 \cdot 10^3$							
5	Unipolar	EF, as-grown	1400	10^9	No data	No data	Au/Cr/ZrO ₂ :Au/n ⁺ -Si, from 100 \times 100 μ m ² to 1000 \times 1000 μ m ²	70 nm, Au-implanted amorphous film, EBE	[26]		
		Set, <i>HRS</i>	1100	$(2-500) \cdot 10^6$							
	Reset, <i>LRS</i>	290	$(1-300) \cdot 10^2$	> 66	SCLC VRH ^V						
	Set, <i>HRS</i>		$(2-500) \cdot 10^6$								
Bipolar	Set, <i>HRS</i>	\pm 570	$(1-300) \cdot 10^2$	SCLC VRH							
	Reset, <i>LRS</i>										
6	Bipolar	EF	No data	$> 10^9$	–	No data	Ag/ZrO ₂ :Cu/ Pt, 0.5 \times 0.5 μ m ²	40 nm, amorphous layer with Cu nanocrystal, EBE	[24]		
		Set, <i>HRS</i>	125	$(1-300) \cdot 10^7$						$> 3 \cdot 10^4$	
		Reset, <i>LRS</i>	-50	200...320							

7	Bipolar	Set, <i>HRS</i> Reset, <i>LRS</i>	420 -80	$9 \cdot 10^4$ 40	$> 2 \cdot 10^3$	SE, Ohm Ohm	Al/ZrO ₂ /Al, Ø 80 µm	60 nm, amorphous stoichiometric film, magnetron sputtering	[22]
8	Bipolar	Set, <i>HRS</i> Reset, <i>LRS</i>	> 600 < -1400	10^5-10^6 10^3	$> 10^2 \dots 10^3$	P-F ^{VI} Ohm	ITO/ZrO ₂ /Ag, 60×60 µm ² , Ag	20...50 nm, solid PC (c ^{XI}) film, sol-gel process	[17]
9	– Bipolar	EF Set, <i>HRS</i> Reset, <i>LRS</i>	850 1000 < -1000	No data 10^6 10^4	– $> 10^2$	No data No data	Cu/ZrO ₂ /TiO ₂ /Ti, no data	50 nm, solid amorphous film, EBE	[23]
10	– Bipolar	EF Set, <i>HRS</i> Reset, <i>LRS</i>	1375 250±50 -250±25	No data No data 130	No data	No data SCLC Ohm	Pt/Ti/ZrO ₂ /Pt/Ti 100×100 µm ²	20 nm, solid film, no data	[25]
11	Unipolar	Set, <i>HRS</i> Reset, <i>LRS</i>	≈ 50 ≈ 10	No data	No data	No data	Ag/ZrO ₂ /Pt, Ø 200 µm, Ag	50 nm, no data, EBE	[18]
12	– Unipolar Bipolar	EF, as- grown Set, <i>HRS</i> Reset, <i>LRS</i> Set, <i>HRS</i> Reset, <i>LRS</i>	≈ 200 ≈ 300 ~140 -(120±20) 200±100	≈ 10^7 ≈ 10^7 ≈ $1.3 \cdot 10^4$ ≈ 10^6 ≈ 10^4	– > 100	No data	Cu/ZrO ₂ /Pt, Ø 200 µm, Cu	50 nm, PC film, EBE	[31]
13	– Unipolar	EF Set, <i>HRS</i> Reset, <i>LRS</i>	6000 (1.6–2.6)· 10^3 (6–13)· 10^2	No data $3 \cdot 10^5$ $2 \cdot 10^2$	– > 10	No data	Ni/ZrO ₂ /TaN, Ø 150 µm	10 nm, PC film, magnetron sputtering	[53]
14	Unipolar Bipolar	Set, <i>HRS</i> Reset, <i>LRS</i> Set, <i>HRS</i> Reset, <i>LRS</i>	1050–1800 400–750 1050–1800 400–750	≈ 10^8 ≈ 10^2 ≈ 10^8 ≈ 10^2	$> 10^6$	No data	Cu/ZrO ₂ :Cu/Pt, from 3×3 µm ² to 20×20 µm ² , Cu	20 nm, Cu-doped layer, EBE	[19]
15	Bipolar	Set, <i>HRS</i> Reset, <i>LRS</i>	≈ 200 ≈ 90	≈ 10^7 ≈ 10^2	$> 10^4$	Complex Ohm	Cu/ZrO ₂ :Ti/Pt, Ti/ZrO ₂ :Ti/Pt, from 50×50 µm ² to 800×800 µm ² , Ti	70 nm, Ti-implanted PC film, EBE	[20]

16	– Bipolar	EF Set, <i>HRS</i> Reset, <i>LRS</i>	≈ 1800 No data	No data	– > 10	No data	TaN/ZrO ₂ /Pt, TaN/ZrO ₂ :Gd/Pt, TaN/ZrO ₂ :Dy/Pt, TaN/ZrO ₂ :Ce/Pt, Ø 100 µm	(13...25) nm, pure, Gd-, Dy- or Ce-doped PC (t and c) film, sol-gel process	[29, 33]
17	Bipolar	Set, <i>HRS</i> Reset, <i>LRS</i>	±75	11.5·10 ³ 263	> 44	SCLC Ohm	ITO/ZrO ₂ :PVP ^{VII} /Ag 100×100 µm ²	200 nm, nanocomposite layer, spin coating	[34]
18	Bipolar	Set, <i>HRS</i> Reset, <i>LRS</i>	≈ (1.5...1.8) ·10 ⁴ ≈ (0.7...1.5) ·10 ⁴	> 130 < 115	> 32 for Ag/ZrO ₂ /ITO, > 1.7 for Ag/ZrO ₂ /Ag	SCLC Ohm	Ag/ZrO ₂ /Ag, Ag/ZrO ₂ /ITO, no data, Ag ⁺	100 nm, PC (m) film, magnetron sputtering	[57]

^I Ohm is Ohmic conduction

^{II} SCLC is space-charge-limited conduction

^{III} SE is Schottky emission

^{IV} EBE is electron beam evaporation

^V VRH is Mott variable range hopping

^{VI} P-F is Poole-Frenkel emission

^{VII} PVP is Poly (4-vinylphenol)

^{VIII} PC is polycrystalline

^{IX} *t* is the tetragonal phase

^X *m* is the monoclinic phase

^{XI} *c* is the cubic phase

Conduction Mechanisms

HRS

Figure 6 shows the $J(E)$ data in double logarithmic coordinates for both resistive switching modes. It is seen that the measured dependencies for HRS contain three linear segments with different tangents of inclination angles. In browsing the literature [58, 59, 60], it can be concluded that the above behavior corresponds to the I - V characteristics of a dielectric with monoenergetic traps capable of filling with injected electrons. The theory of injection currents reads that such systems can implement the space-charge-limited conduction (SCLC) mechanism [58]. The SCLC model succeeds at describing carrier transport through a dielectric layer by the following equations [58, 59, 60]:

$$J_{Ohm} = \frac{I_{Ohm}}{S} = e\mu n_0 \frac{U}{d} = e\mu n_0 E, \quad (1)$$

$$J_{TFL} = \frac{I_{TFL}}{S} = \frac{9}{8} \mu_{eff} \varepsilon \varepsilon_0 \frac{U^2}{d^3} = \frac{9}{8} \mu_{eff} \varepsilon \varepsilon_0 \frac{E^2}{d}, \quad (2)$$

$$\mu_{eff} = \mu \theta, \quad (3)$$

$$\tau_c = \frac{d^2}{\mu_{eff} U_{tr}} = \frac{d}{\mu_{eff} E_{tr}}, \quad (4)$$

$$\tau_d = \frac{\varepsilon \varepsilon_0}{en \mu_{eff}}, \quad (5)$$

$$E_{TFL} = \frac{U_{TFL}}{d} = \frac{e N_t d}{2 \varepsilon \varepsilon_0}, \quad (6)$$

where J_{Ohm} is Ohm's law current density, A/cm²; I_{Ohm} is Ohm's law current, A/cm²; S is the memristor area, cm²; e is the electron charge, C; μ is the electronic drift mobility, cm²/(V·s); n_0 is carrier concentration in thermal equilibrium, cm⁻³; U is applied voltage, V; d is the thickness of oxide layer, cm; E is applied electric field, V/cm; J_{TFL} is trap-filled limit current density, A/cm²; I_{TFL} is trap-filled limit current, A; μ_{eff} is effective electron mobility, cm²/(V·s); ε is the static dielectric constant; ε_0 is the permittivity in vacuum, F/cm; θ is the ratio of the free carrier density to total carrier density; τ_c is carrier transit time, s; U_{tr} is transition voltage, V; E_{tr} is transition electric field, V/cm; τ_d is dielectric relaxation time, s; n is the concentration of the free carriers in the oxide, cm⁻³; E_{TFL} is the trap-filled limit electric field, V/cm; U_{TFL} is the trap-filled limit voltage, V; N_t is the trap density, cm⁻³.

In our case, electrons are the charge carriers in the ZrO₂-nt layer, and oxygen vacancies V_{OS} are traps. From now on, when discussing experimental data within the SCLC model [58, 59, 60], we will adhere to this statement.

For $E < E_{tr}$, the $J(E)$ dependence is linear ($J_{Ohm} \sim E$) and obeys Ohm's law in Eq. (1). Such a regime for ZrO₂ is typical of an electrically quasi-neutral state that corresponds to the early stage of filling the V_{OS} at weak injection $N_{t0} \rightarrow 0$.

In the case of $E = E_{tr}$, the number of injected and free electrons in the active memristor layer coincides ($n = n_0$), and the transit times (see Eq. (4)) and electron relaxation (see Eq. (5)) are equal, i.e. $\tau_c = \tau_d$. Moreover, $\theta \rightarrow 1$ since the number of filled traps is $N_{t,0} \rightarrow 0$.

For $E_{tr} < E < E_{TFL}$, the condition of strong injection holds. In the concerned range of E , the traps continue filling up, and the dependence becomes quadratic ($J_{TFL} \sim E^2$). As E grows, the concentration of free injected electrons increases, which in turn leads to a shift in the position of the Fermi quasi-level to the position of the level of traps in the bandgap.

For $E \geq E_{TFL}$, the current flowing through the structure abruptly goes up, and the double logarithmic dependence $J(E)$ has a slope $k \geq 3$ ($J \sim E^k$). This fact evidences the complete filling of

traps and the possibility of freely moving the injected electrons in the ZrO_2 layer. Thus, the E_{TFL} strength matches the V_O levels completely filled (see Eq. (6)) and (or) the coincidence of the positions of the Fermi quasi-levels and monoenergetic V_O levels in the bandgap [58, 59]. Then, a very strong injection is the reason for CFs to form in the electric field range in question.

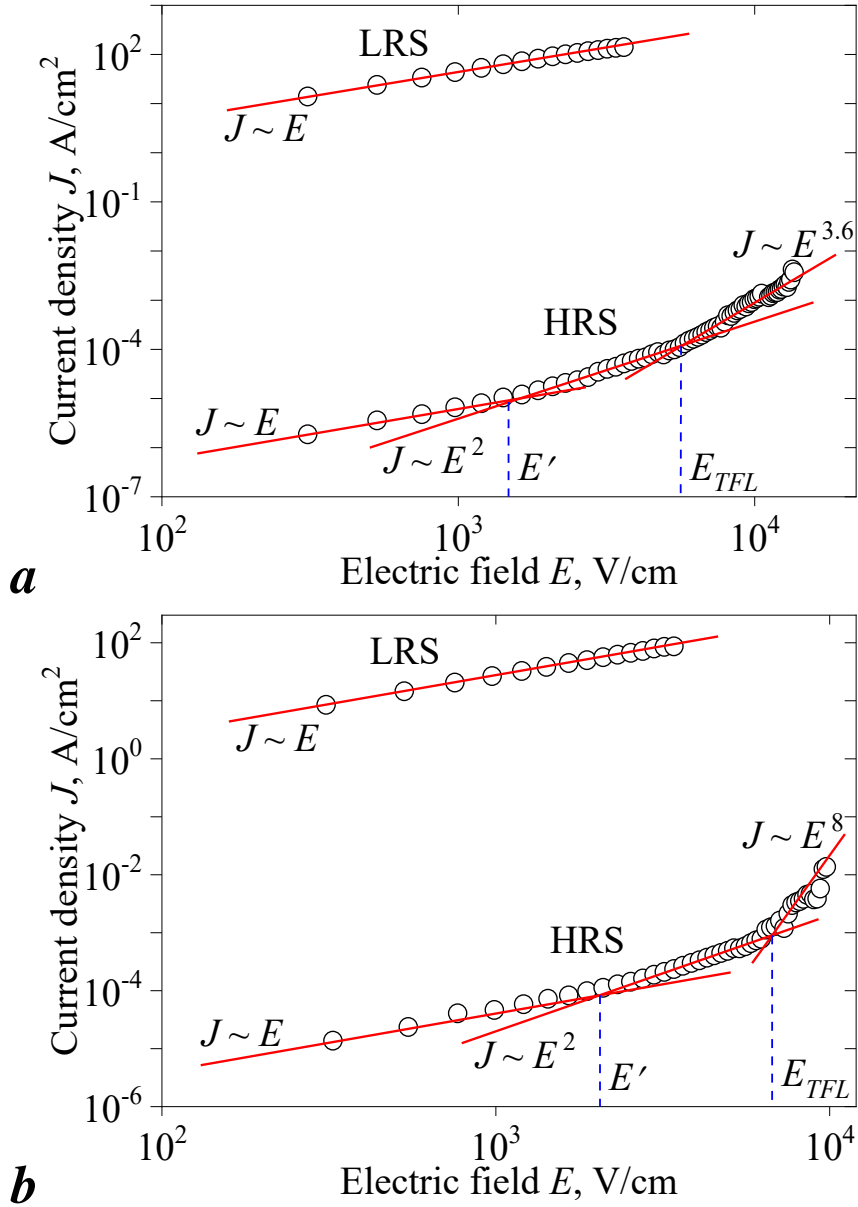


Figure 6. Dependencies of current density (J) on strength (E) in double logarithmic coordinates for bipolar (a) and unipolar (b) switching modes. Symbols are the experimental data. Solid lines represent a linear approximation.

To evaluate the parameters of the ZrO_2 -nt layer using Eq. (1) – (6), we measured the electric capacitance of memristors in *HRS*, which amounted to $C = 1$ pF. In the case of the geometry of a flat capacitor, we obtain the relative permittivity of $\epsilon = 20 \pm 2$. This value is quite consistent with $\epsilon = 14 - 40$ for continuous thin zirconium films [28, 61, 62] and coincides with the estimate of $\epsilon = 21$ for an anodized ZrO_2 layer synthesized in a galvanostatic mode at room temperature in an electrolyte of ammonium tetraborate [63]. Here, the morphology of the oxide layer is not covered.

The electric and physical characteristics of the ZrO_2 -nt layer in *HRS*: $\mu_{eff} \approx \mu = (0.1 - 12) \cdot 10^{-3} \text{ cm}^2 \cdot (\text{V} \cdot \text{s})^{-1}$, $N_t = (1 - 3) \cdot 10^{15} \text{ cm}^{-3}$, $\tau_c = 0.3 - 1.3 \text{ ms}$ and $n_0 = (1 - 3) \cdot 10^{14} \text{ cm}^{-3}$ were calculated according to Eq. (1) – (6). It is seen that the mobility values obtained at room temperature are

comparable with independent estimates of $\mu = 23 \cdot 10^{-3}$ [64] and $5.8 \cdot 10^{-3} \text{ cm}^2 \cdot (\text{V} \cdot \text{s})^{-1}$ [65] at $900 \text{ }^\circ\text{C}$ for single-crystal ZrO_2 stabilized Y_2O_3 .

It is important to note that, in a number of independent works, both theory and experiment confirm a high concentration of V_O in various anodized oxides [38,63,66,67,68,69]. For example, when treated at a temperature of $500 \text{ }^\circ\text{C}$ for 4 h in a reducing atmosphere of 5% H_2/N_2 , TiO_2 nanotubular array increases the concentration of active surface defects, with the charge carrier density becoming equal to $9.86 \cdot 10^{20} \text{ cm}^{-3}$ [68]. Large values of $2.5 \cdot 10^{21} \text{ cm}^{-3}$ for the V_O concentration in ZrO_2 single crystals stabilized by Y_2O_3 were previously determined by the electron paramagnetic resonance (EPR) method [65].

The significantly lower value of $N_t = (1 - 3) \cdot 10^{15} \text{ cm}^{-3}$, obtained in the present work can be explained by the presence of F^- ions. It is known that fluorine substitutes for oxygen vacancies in ionic crystals, which leads to a decrease in the concentration of V_O and eliminates allowed capture levels in the bandgap of oxides [70]. X-ray fluorescence and photoelectron spectroscopy methods confirm the presence of fluorine in the samples under study. The fluorine and hafnium contents are found to amount to 2.5 and 1 at. %, respectively.

LRS

It is clear from Figure 6 that, for a low resistive state, all the $J(E)$ dependencies in double logarithmic coordinates are linear with the slope tangent ≈ 1 ($J_{Ohm} \sim E$), which corresponds to Ohm's law. Such a behavior is also typical of memristor structures based on continuous ZrO_2 layers in LRS (see Table 1) [16, 17, 20, 22, 25, 34]. In addition, the I - V curves have a region of switching at $U = 0.4 - 1 \text{ V}$ during the LRS \rightarrow HRS transition. In this case, the G conductance of the memristor structure stepwise decreases. For example, with increasing U , the magnitude of G diminishes by a factor to one-half and half-integer values of the quantum of electrical conductance $G_0 = 2e^2/h \approx 77.5 \text{ } \mu\text{S}$ (Figure 7, curve X) in the row: $53G_0 \rightarrow 51G_0 \rightarrow 48G_0 \rightarrow 45G_0 \rightarrow 13G_0 \rightarrow 9G_0 \rightarrow 5G_0 \rightarrow 4G_0 \rightarrow 3G_0 \rightarrow 2G_0 \rightarrow 1.5G_0 \rightarrow 1G_0 \rightarrow 0.5G_0 \rightarrow G_{HRS}$.

The resistive switching of various memristor structures as a result of the formation of quantum conductive filaments (QCFs) at room temperature is an experimentally and theoretically confirmed fact [71 and ref. in it]. For example, it is established in [31] that quantum conductive filaments (QCFs) in $\text{Cu}/\text{ZrO}_2/\text{Pt}$ memristors are formed in a controlled manner.

Based on the experimental R_{LRS} values (see Table 1), it can be argued that when performing the "EF" and "Set" operations, tens and hundreds of QCFs are formed and restored between the electrodes in memristors. This corresponds to the formation of one QCF per 10^4 - 10^5 ZrO_2 nanotubes, whereas their number in the memristor is $\approx 3.5 \cdot 10^6$ pieces. It is safe to say that QCFs fully determine electron transport through the memristor in the LRS, and the discreteness of the change in the conductance values leads to the quantization of the mobility values.

Let one QCF have a volume V_{QCF} , in which two electrons reside. Then, according to Eq. (1), the mobility of elementary charges in LRS is discrete:

$$\mu_{LRS} = \mu_0 \frac{xV_{QCF}}{Sd}, \quad (7)$$

Where $\mu_0 = ed^2/h \approx 698.7 \text{ m}^2 \cdot (\text{V} \cdot \text{s})^{-1}$. The data of speculations are consistent with theoretical calculations of electron mobility in multi-walled carbon nanotubes within an ideal multi-box model, for which μ is quantized and proportional to the square of the nanotube length [72].

Eq.(7) implies that μ_{LRS} depends on the ratio of the geometric dimensions of the memristor and QCF, as well as the number of filaments formed. So, comparing the volumes of memristor and QCFs ($Sd \rightarrow x V_{QCF}$), we get that $\mu_{LRS} \rightarrow \mu_0$. Thus, a possible increase in electron mobility in ZrO_2 -nt during the transition of the memristor from HRS to LRS is a result of the quantization of energy states in one-dimensional channels arising from the motion of charge carriers over QCFs in a dielectric layer. It was previously reported that $\mu = 12$ - $13 \text{ cm}^2 \cdot (\text{V} \cdot \text{s})^{-1}$ at temperatures of 425 - 475K

for thin amorphous oxide films in the Al/ZrO₂/p-Si structure using the modified Schottky emission model [73].

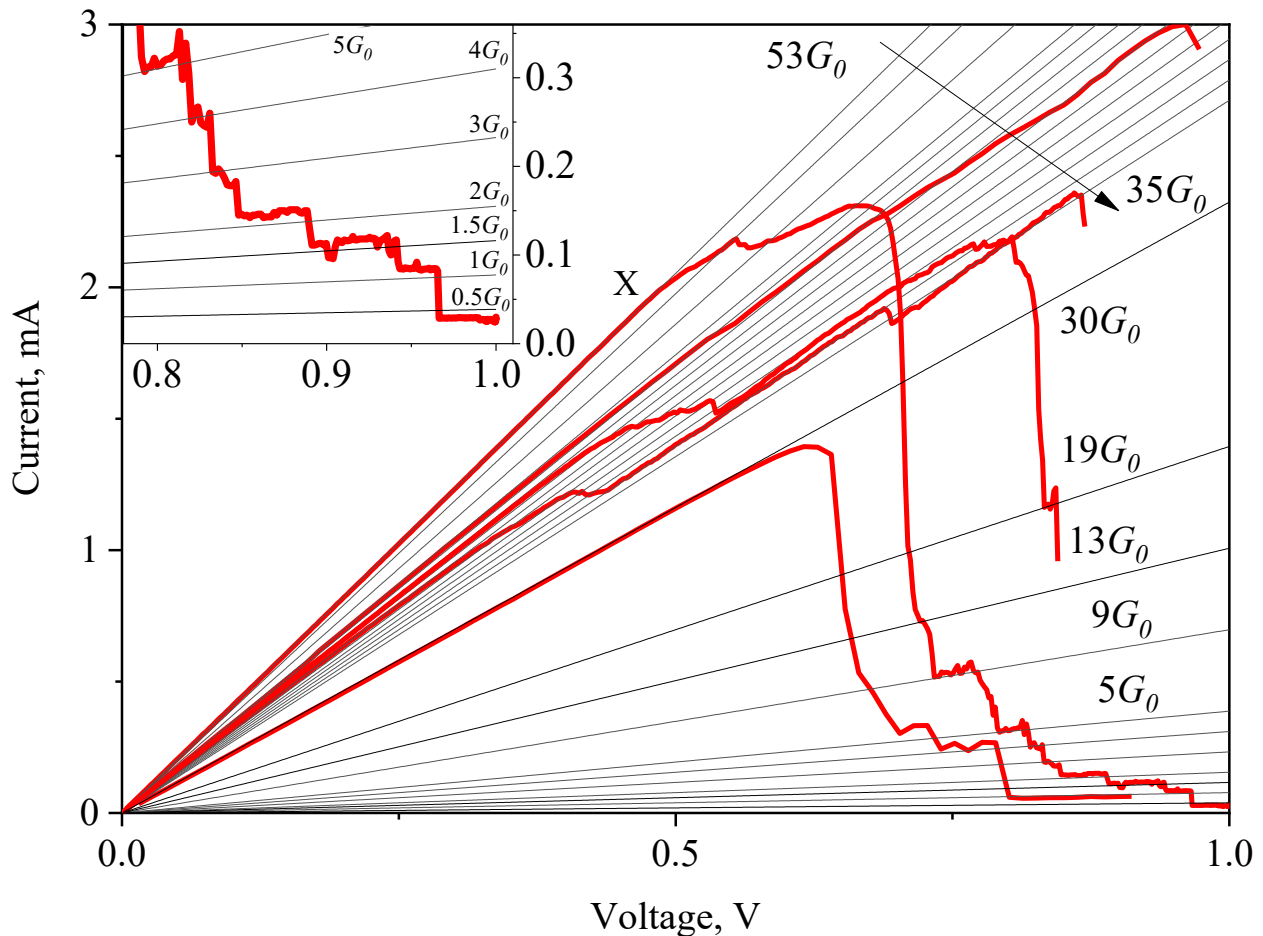


Figure 7. Experimental I - V characteristics of memristors in LRS (solid red lines) and a series of theoretical I - V characteristics for CFs with quantum conductance xG_0 (thin black lines), where x is the number of QCFs and $G_0 = 2e^2/h \approx 77.5 \mu\text{S}$ is the quantum of electrical conductance.

It should be underscored that the generated QCFs in the ZrO₂-nt layer are stable even at room temperature and retain their conducting state when E is turned off. Subsequently, during the “Reset” operation, QCFs are destroyed. Next, we explain the mechanisms of electroforming and resistive switching of memristors with the participation of V_O²⁺ oxygen vacancies, O²⁻ oxygen and F⁻ fluorine ions in these processes.

Resistive Switching Mechanisms

Figure 8 schematically sketches the processes that occur in nanotubes in the bipolar memristive switching mode. The as-grown nanotube whose fragment is outlined by a dark frame has increased non-stoichiometry in oxygen at the ZrO₂-nt/Zr interface [38, 66, 74]. Independent data on the ZrO₂-nt layer, obtained by transmission electron microscopy and energy dispersive X-ray analysis, show that the content of F⁻ ions is also high in this region [74].

When electroforming (see Figure 8, operations EF), several complementary processes can proceed in the Zr/ZrO₂-nt/Au structure at hand. Firstly, positively charged oxygen vacancies V_O²⁺ migrate outwards and towards the Au-contact in an applied electric field at $E > 0$ and $E < 0$, respectively. The aforementioned vacancy centers have a positive charge relative to the crystal lattice, and their motion appears to obey the exchange mechanism in the anion sublattice due to the diffusion of O²⁻ [75] and F⁻ ions along the grain boundaries of the nanotubes in an external electric field.

Secondly, the motion of negatively charged F^- and/or O^{2-} ions outwards and towards the Au contact is initiated at $E > 0$ and $E < 0$, respectively. In this case, extra oxygen vacancies emerge in the ZrO_2 nanotubes. It is known that the mobility of fluorine in anodized oxides is almost twice that of oxygen [76, 77]. Consequently, the transition of F from the O position to the F_i^- -interstice in an external electric field results in V_O -forming as a most probable process. The latter proceeds according to the $F_O^- \rightarrow V_O^{2+} + F_i^-$ mechanism [70]. It should be underscored that the diffusion of O and the formation of voids at the “active layer/electrode” interface during the EF process were experimentally confirmed by studying the distribution of chemical elements in a Pt/TiO₂/Pt memristor using two-dimensional energy-dispersive X-ray spectroscopy [78].

Thus, the QCFs are formed upon locally reaching a certain threshold concentration of V_O in the ZrO_2 -nt layer, and the memristor passes into the *LRS* state (see Figure 8, a red frame). It is worth emphasizing that the EF process for memristors at $E < 0$ is less energy-consuming as compared to that at $E > 0$ since it proceeds at lower E_{EF} values (see Table 1).

Further, resistive switching is possible to implement after the mandatory EF procedure. So when placing the memristor being in the *LRS* into an electric field E , current flows through the QCFs formed. Once heated up due to the Joule heat, they are locally destroyed as a result of diffusion of V_O , F and/or O (see Figure 8, Reset operation). Chances are, the QCFs collapse, first of all, inside the nanotube walls far from the metal contacts, and the memristor passes into the *HRS* state (see Fig. 8, a blue frame). Subsequently, the applied field E initiates the diffusion process of V_O , F, and/or O in locally destroyed areas of the QCFs (see Figure 8, operation Set). When restored, the V_O chains make the memristor go into the *LRS* state. As it becomes clear from Table 1, $E_{SET} > E_{RES}$ for both switching modes of the memristors tested. Thus, partial destruction of the QCFs in the active layer requires less energy than their restoration. The similar behavior of the Zr/ZrO₂-nt/Au structure is consistent with a number of independent works [16, 21, 22, 24, 26, 49] for continuous-ZrO₂ layer-based memristors.

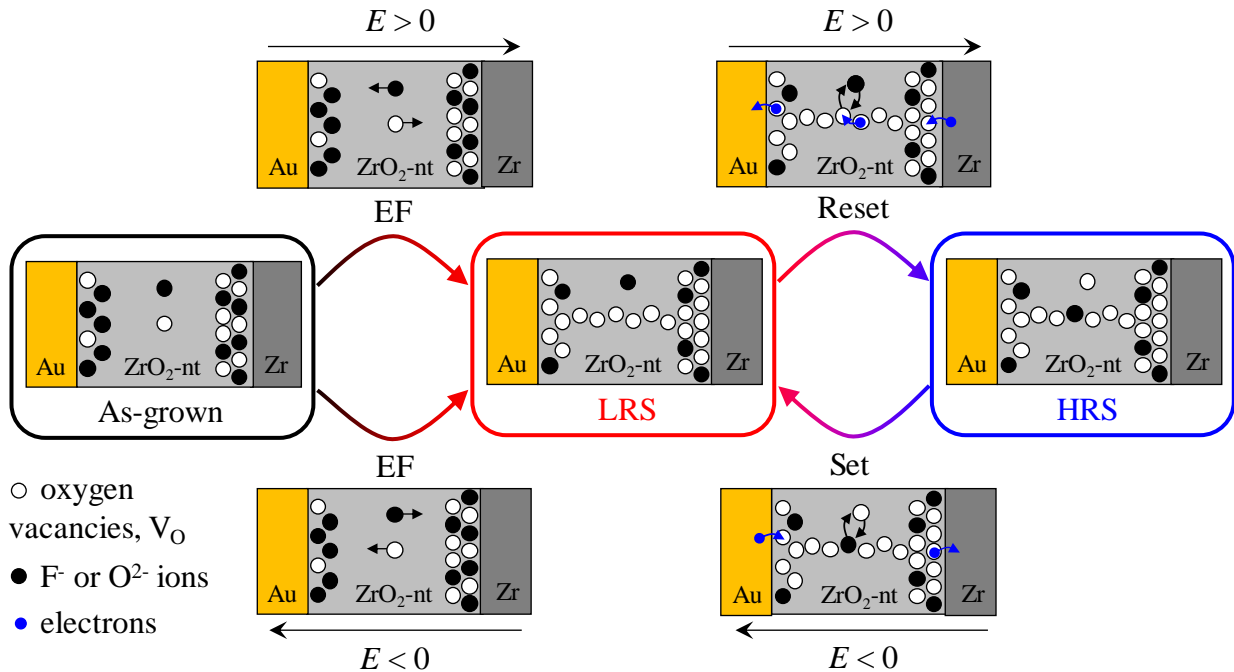


Figure 8. Schematic representation of the processes of formation (EF), destruction (Reset), and restoration (Set) of a quantum conductive filament in a ZrO_2 nanotube for a bipolar switching mode. Detailed explanations for the figure are given in the text.

Conclusion

Memristor structures based on a 1.7 μm thick ZrO_2 nanotubular layer synthesized by anodic oxidation were fabricated. An analysis of SEM images showed that the oxide layer consists of an ordered array of vertically oriented nanotubes with average internal and external diameters of 55 and 75 nm, respectively.

The I - V curves of the $\text{Zr}/\text{ZrO}_2\text{-nt}/\text{Au}$ memristors investigated exhibit a unipolar and bipolar mechanisms of the $LRS \leftrightarrow HRS$ resistive switching over several tens of complete switching cycles. The ranges of changes in the resistances of the synthesized structures, $R_{HRS} \geq 8 \text{ M}\Omega$ and $R_{LRS} \leq 450 \Omega$, as well as the ratio $R_{HRS} / R_{LRS} \geq 3 \cdot 10^4$, were determined. Based on the analysis of the I - V curves, it can be inferred that the conductivity either of the ohmic type or limited by space charge (SCLC) is realized in the LRS and HRS states, respectively. The effective carrier mobility $\mu_{\text{eff}} = (0.1\text{-}12) \cdot 10^{-3} \text{ cm}^2/(\text{V}\cdot\text{s})$ in the studied structure was calculated. The concentration of charge carrier traps based on oxygen vacancies, $N_t = (1\text{-}3) \cdot 10^{15} \text{ cm}^{-3}$, in the non-stoichiometric nanotubular ZrO_{2-x} layer was estimated. The prospects of using the $\text{Zr}/\text{ZrO}_2\text{-nt}/\text{Au}$ layered structure as a functional medium for memristor memory elements, as well as possible trends for improving their functional characteristics, are shown.

Acknowledgements

The work was supported by Minobrnauki research project FEUZ-2020-0059. Authors thank I.N. Bainov for help in XRD measurements.

References

- [1] Minh N.Q. Ceramic Fuel Cells // Journal of the American Ceramic Society, Volume 76, Issue 3, March 1993, Pages 563-588. <https://doi.org/10.1111/j.1151-2916.1993.tb03645.x>
- [2] Ishihara T., Sato K., Takita Y. Electrophoretic deposition of Y_2O_3 -stabilized ZrO_2 electrolyte films in solid oxide fuel cells // Journal of the American Ceramic Society, Volume 79, Issue 4, April 1996, Pages 913-919. <https://doi.org/10.1111/j.1151-2916.1996.tb08525.x>
- [3] Birkby I. and Stevens R. Applications of Zirconia Ceramics // Key Engineering Materials, Vols. 122-124, pp. 527-552, 1996. <https://doi.org/10.4028/www.scientific.net/KEM.122-124.527>
- [4] Petrik N.G., Taylor D.P., Orlando T.M. Laser-stimulated luminescence of yttria-stabilized cubic zirconia crystals, Journal of Applied Physics, Volume 85, Issue 9, 1 May 1999, Pages 6770-6776 <https://doi.org/10.1063/1.370192>
- [5] Yadav G.D., Nair J.J. Sulfated zirconia and its modified versions as promising catalysts for industrial processes, Microporous and Mesoporous Materials, Volume 33, Issue 1-3, 15 December 1999, Pages 1-48 [https://doi.org/10.1016/S1387-1811\(99\)00147-X](https://doi.org/10.1016/S1387-1811(99)00147-X)
- [6] Herrmann J.-M. Heterogeneous photocatalysis: State of the art and present applications, Topics in Catalysis, Volume 34, Issue 1-4, May 2005, Pages 49-65 <https://doi.org/10.1007%2Fs11244-005-3788-2>
- [7] Kozhevina A.V., Vokhmintsev A.S., Kamalov R.V., Martemyanov N.A., Chukin A.V., Weinstein I.A. Optical absorption edge parameters of zirconium dioxide nanotubular structures // Journal of Physics: Conference Series, Volume 917, Issue 6, 23 November 2017, Article number 062031. <https://doi.org/10.1088/1742-6596/917/6/062031>
- [8] Romero V.H., De la Rosa E., López-Luke T., Salas P., Angeles-Chavez C. Brilliant blue, green and orange-red emission band on Tm^{3+} -, Tb^{3+} - and Eu^{3+} -doped ZrO_2 nanocrystal // Journal of Physics D: Applied Physics, Volume 43, Issue 46, 24 November 2010, Article number 465105 <https://doi.org/10.1088/0022-3727/43/46/465105>

-
- [9] P. Salas, E. De la Rosa-Cruz, L.A. Diaz-Torres, V.M. Castaño, R. Meléndrez, M. Barboza-Flores “Monoclinic ZrO₂ as a broad spectral response thermoluminescence UV dosimeter”, *Radiation Measurements*, Volume 37, Issue 2, April 2003, Pages 187-190 [https://doi.org/10.1016/S1350-4487\(02\)00174-9](https://doi.org/10.1016/S1350-4487(02)00174-9)
- [10] Nikiforov S.V., Kortov V.S., Savushkin D.L., Vokhmintsev A.S., Weinstein I.A. Thermal quenching of luminescence in nanostructured monoclinic zirconium dioxide // *Radiation Measurements*, Volume 106, November 2017, Pages 155-160. <https://doi.org/10.1016/j.radmeas.2017.03.020>
- [11] Shin H., Jeong D.-K., Lee J., Sung M.M., Kim J. Formation of TiO₂ and ZrO₂ nanotubes using atomic layer deposition with ultraprecise control of the wall thickness // *Advanced Materials*, Volume 16, Issue 14, 19 July 2004, Pages 1197-1200. <https://doi.org/10.1002/adma.200306296>
- [12] H. Yan, H.S. Choe, S. Nam, Y. Hu, S. Das, J.F. Klemic, J.C. Ellenbogen, C.M. Lieber Programmable nanowire circuits for nanoprocessors, *Nature*, Volume 470, Issue 7333, 10 February 2011, Pages 240-244 <https://doi.org/10.1038/nature09749>
- [13] Ha Y.-G., Everaerts K., Hersam M.C., Marks T.J. Hybrid gate dielectric materials for unconventional electronic circuitry // *Accounts of Chemical Research*, Volume 47, Issue 4, 15 April 2014, Pages 1019-1028. <https://doi.org/10.1021/ar4002262>
- [14] Manicone P.F., Rossi Iommetti P., Raffaelli L. An overview of zirconia ceramics: Basic properties and clinical applications // *Journal of Dentistry*, Volume 35, Issue 11, November 2007, Pages 819-826. <https://doi.org/10.1016/j.jdent.2007.07.008>
- [15] Hisbergues M., Vendeville S., Vendeville P. Review zirconia: Established facts and perspectives for a biomaterial in dental implantology // *Journal of Biomedical Materials Research - Part B Applied Biomaterials*, Volume 88, Issue 2, February 2009, Pages 519-529. <https://doi.org/10.1002/jbm.b.31147>
- [16] Lee D., Choi H., Sim H., Choi D., Hwang H., Lee M.-J., Seo S.-A., Yoo, I.K. Resistance switching of the nonstoichiometric zirconium oxide for nonvolatile memory applications // *IEEE Electron Device Letters*, Volume 26, Issue 10, October 2005, Pages 719-721. <https://doi.org/10.1109/LED.2005.854397>
- [17] S. Lee, T. Kim, B. Jang, W.-Y. Lee, K.C. Song, H.S. Kim, G.Y. Do, S.B. Hwang, S. Chung and J. Jang “Impact of Device Area and Film Thickness on Performance of Sol-Gel Processed ZrO₂ RRAM” 2018 *IEEE Electron Device Lett.* **39** 668 <https://doi.org/10.1109/LED.2018.2820141>
- [18] Du G., Wang C., Li H., Mao Q., Ji Z. Bidirectional threshold switching characteristics in Ag/ZrO₂/Pt electrochemical metallization cells // *AIP Advances* 6, 085316 (2016). <https://doi.org/10.1063/1.4961709>
- [19] Guan W., Long S., Liu Q., Liu M., Wang W. Nonpolar Nonvolatile Resistive Switching in Cu Doped ZrO₂ // *IEEE Electron Device Letters*, Volume 29, Issue 5, May 2008, Pages 434-437. DOI: 10.1109/LED.2008.919602. <https://ieeexplore.ieee.org/document/4494620>
- [20] Liu Q., Long S., Wang W., Zuo Q., Zhang S., Chen J., Liu M. Improvement of resistive switching properties in ZrO₂-Based ReRAM with implanted Ti ions // *IEEE Electron Device Letters*, Volume 30, Issue 12, December 2009, Pages 1335-1337. DOI: 10.1109/LED.2009.2032566. <https://ieeexplore.ieee.org/document/5332367>
- [21] Kundozerova T.V., Stefanovich G.B., Grishin A.M. Binary anodic oxides for memristor-type nonvolatile memory // *Physica Status Solidi (C) Current Topics in Solid State Physics*, Volume 9, Issue 7, July 2012, Pages 1699-1701. <https://doi.org/10.1002/pssc.201100625>

-
- [22] Wu X., Zhou P., Li J., Chen L.Y., Lv H.B., Lin Y.Y., Tang T.A. Reproducible unipolar resistance switching in stoichiometric ZrO₂ films // *Appl. Phys. Lett.* **90** 183507 (2007). <https://doi.org/10.1063/1.2734900>
- [23] Li Y., Yuan P., Fu L., Li R., Gao X. and Tao C. Coexistence of diode-like volatile and multilevel nonvolatile resistive switching in a ZrO₂/TiO₂ stack structure, 2015 *Nanotechnol.* **26** 391001. <https://doi.org/10.1088/0957-4484/26/39/391001>
- [24] Liu Q., Long S., Lv H., Wang W., Niu J., Huo Z., Chen J., Liu M. Controllable Growth of Nanoscale Conductive Filaments in Solid-Electrolyte-Based ReRAM by Using a Metal Nanocrystal Covered Bottom Electrode // 2010 *ACS Nano* **4** 10. <https://doi.org/10.1021/nn1017582>
- [25] Lei X.-Y., Liu H.-X., Gao H.-X., Yang H.-N., Wang G.-M., Long S.-B., Ma X.-H. and Liu M. “Resistive switching characteristics of Ti/ZrO₂/Pt RRAM device” 2014 Chinese Physics B Volume 23, Issue 11, 1 November 2014, Article number 117305. <http://dx.doi.org/10.1088/1674-1056/23/11/117305>
- [26] Liu Q., Guan W., Long S., Liu M., Zhang S., Wang Q. and Chen J. Resistance switching of Au-implanted-ZrO₂ film for nonvolatile memory application, 2008 *J. Appl. Phys.* **104** 114514. <https://doi.org/10.1063/1.3033561>
- [27] Yildirim H., Pachter R. Extrinsic Dopant Effects on Oxygen Vacancy Formation Energies in ZrO₂ with Implication for Memristive Device Performance // *ACS Appl. Electron. Mater.* 2019, 1, 467–477. <https://doi.org/10.1021/acsaelm.8b00090>
- [28] Panda D., Tseng T.Y. Growth, dielectric properties, and memory device applications of ZrO₂ thin films // *Thin Solid Films*, Volume 531, 15 March 2013, Pages 1-20. <https://doi.org/10.1016/j.tsf.2013.01.004>
- [29] Lee M.S., Choi S., An C.-H., Kim H. Resistive switching characteristics of solution-deposited Gd, Dy, and Ce-doped ZrO₂ films // *Applied Physics Letters*, Volume 100, Issue 14, 2 April 2012, Article number 143504. <https://doi.org/10.1063/1.3700728>
- [30] Yang J.J., Strukov D.B., Stewart D.R. Memristive devices for computing // *Nature Nanotechnology*, Volume 8, 2013, Pages 13–24. <https://doi.org/10.1038/NNANO.2012.240>
- [31] Du G., Li H., Mao Q., Ji Z. Controllable volatile to nonvolatile resistive switching conversion and conductive filaments engineering in Cu/ZrO₂/Pt devices // *Journal of Physics D: Applied Physics*, Volume 49, Issue 44, 13 October 2016, Article number 445105. <https://doi.org/10.1088/0022-3727/49/44/445105>
- [32] Petrenyov I.A., Vokhmintsev A.S., Kamalov R.V., Weinstein I.A. Conduction mechanisms in memristors based on nanotubular arrays of zirconium oxide // *AIP Conference Proceedings*, Volume 2174, 6 December 2019, Article number 020242. <https://doi.org/10.1063/1.5134393>
- [33] Lee M.S., An C.-H., Park K., Choi J.-Y., Kim H. Effect of Y, Gd, Dy, and Ce Doping on the Microstructural and Electrical Properties of Sol-Gel-Deposited ZrO₂ Film // *Journal of the Electrochemical Society*, 158(6), Pages G133-G136. <https://doi.org/10.1149/1.3562971>
- [34] Khan M.U., Hassan G. and Bae J. Non-volatile resistive switching based on zirconium dioxide: poly (4-vinylphenol) nano-composite, 2019 *Appl. Phys. A Mater. Sci. Process.* **125** 378 <https://doi.org/10.1007/s00339-019-2659-9>
- [35] Awais M.N., Choi K.H. Resistive switching mechanism in printed non-volatile Ag/ZrO₂/ITO sandwiched structure // *Electronics Letters* Volume 51, Issue 25, 10 December 2015, Pages 2147-2149 <http://dx.doi.org/10.1049/el.2014.2517>
- [36] Liu Q., Guan W., Long S., Jia R., Liu M., Chen J. Resistive switching memory effect of ZrO₂ films with Zr⁺ implanted // *Appl. Phys. Lett.* **92** 012117 (2008). <https://doi.org/10.1063/1.2832660>

-
- [37] Vokhmintsev A.S., Kamalov R.V., Kozhevina A.V., Petrenyov I.A., Martemyanov N.A., Weinstein I.A. Unidirectional synapse-like behavior of Zr/ZrO₂-NT/Au layered structure // Proceedings - 2018 Ural Symposium on Biomedical Engineering, Radioelectronics and Information Technology, USBEREIT 2018, Pages 348-351. <https://doi.org/10.1109/USBEREIT.2018.8384620>
- [38] Trivinho-Strixino F., Guimarães F.E.G., Pereira E.C. Zirconium oxide anodic films: Optical and structural properties // Chemical Physics Letters, Volume 461, Issue 1-3, 8 August 2008, Pages 82-86. <https://doi.org/10.1016/j.cplett.2008.06.072>
- [39] Yoo J.E., Lee K., Tighineanu A., Schmuki P. Highly ordered TiO₂ nanotube-stumps with memristive response // Electrochemistry Communications, Volume 34, 2013, Pages 177-180. <https://doi.org/10.1016/j.elecom.2013.05.038>
- [40] Valeeva A.A., Kozlova E.A., Vokhmintsev A.S., Kamalov R.V., Dorosheva I.B., Saraev A.A., Weinstein I.A., Rempel, A.A. Nonstoichiometric titanium dioxide nanotubes with enhanced catalytic activity under visible light // Scientific Reports, Volume 8, Issue 1, 1 December 2018, Article number 9607. <https://doi.org/10.1038/s41598-018-28045-1>
- [41] Valeeva A.A., Dorosheva I.B., Kozlova E.A., Kamalov R.V., Vokhmintsev A.S., Selishchev D.S., Saraev A.A., Gerasimov E.Y., Weinstein I.A., Rempel A.A. Influence of calcination on photocatalytic properties of nonstoichiometric titanium dioxide nanotubes // Journal of Alloys and Compounds, Volume 796, 5 August 2019, Pages 293-299. <https://doi.org/10.1016/j.jallcom.2019.04.342>
- [42] Petrenyov I.A., Kamalov R.V., Vokhmintsev A.S., Martemyanov N.A., Weinstein I.A. Nanostructural features of anodic zirconia synthesized using different temperature modes // Journal of Physics: Conference Series, Volume 1124, 2018, Article number 022004. <https://doi.org/10.1088/1742-6596/1124/2/022004>
- [43] Miller K., Nalwa K.S., Bergerud A., Neihart N.M., Chaudhary S. Memristive behavior in thin anodic titania // IEEE Electron Device Letters, Volume 31, Issue 7, July 2010, Article number 5473038, Pages 737-739. <https://doi.org/10.1109/LED.2010.2049092>
- [44] Vokhmintsev A.S., Weinstein I.A., Kamalov R.V., Dorosheva I.B. Memristive effect in a nanotubular layer of anodized titanium dioxide // Bulletin of the Russian Academy of Sciences: Physics, Volume 78, Issue 9, 2014, Pages 932-935. <https://doi.org/10.3103/S1062873814090317>
- [45] Conti D., Lamberti A., Porro S., Rivolo P., Chiolerio A., Pirri C.F., Ricciardi C. Memristive behaviour in poly-acrylic acid coated TiO₂ nanotube arrays // Nanotechnology, Volume 27, Issue 48, 7 November 2016, Article number 485208. <https://doi.org/10.1088/0957-4484/27/48/485208>
- [46] Dorosheva I.B., Vokhmintsev A.S., Kamalov R.V., Gryaznov A.O., Weinstein I.A. Oxide layer thickness effects on the resistance switching characteristics of Ti/TiO₂-NT/Au structure // Proceedings - 2018 Ural Symposium on Biomedical Engineering, Radioelectronics and Information Technology, USBEREIT 2018, 13 June 2018, Pages 279-282. <https://doi.org/10.1109/USBEREIT.2018.8384604>
- [47] Chen J., Wu Y., Zhu K., Sun F., Guo C., Wu X., Cheng G., Zheng R. Core-shell copper nanowire-TiO₂ nanotube arrays with excellent bipolar resistive switching properties // Electrochimica Acta, Volume 316, 1 September 2019, Pages 133-142. <https://doi.org/10.1016/j.electacta.2019.05.110>
- [48] Hazra A., Jan A., Tripathi A., Kundu S., Boppidi P.K.R., Gangopadhyay S. Optimized resistive switching in TiO₂ nanotubes by modulation of oxygen vacancy through chemical reduction // IEEE Transactions on Electron Devices, Volume 67, May 2020, Article number 9064714, Pages 2197-2204. <https://doi.org/10.1109/TED.2020.2983755>

-
- [49] Kundozerova T., Stefanovich G. Resistance switching in metal oxide thin films and its memory application // *Applied Mechanics and Materials*, Volume 346, 2013, Pages 29-34. <https://doi.org/10.4028/www.scientific.net/AMM.346.29>
- [50] Gryaznov A.O., Dorosheva I.B., Vokhmintsev A.S., Kamalov R.V., Weinstein I.A. Automatized complex for measuring the electrical properties of MIM structures // *2016 SIBCON 2016 Proc.* 7491772. <https://ezproxy.urfu.ru:3055/10.1109/SIBCON.2016.7491772>
- [51] Ackermann O.R.J., Garg S.P., Rauh E.G. High-Temperature Phase Diagram for the System Zr // *Journal of the American Ceramic Society* Volume 60, Issue 7-8, July 1977, Pages 341-345. <https://doi.org/10.1111/j.1151-2916.1977.tb15557.x>
- [52] Gabelkov S.V., Tarasov R.V., Poltavtsev N.S., Kryshchal A.P., Pilipenko A.V., Mironova A.G. Low-temperature sintering of yttria-stabilized zirconia produced from amorphous powders // *Powder Metallurgy and Metal Ceramics* Volume 50, Issue 5-6, September 2011, Pages 338-344. <https://doi.org/10.1007/s1106-011-9337-6>
- [53] Tsai T.-L., Ho T.-H. and Tseng T.-Y. Unipolar resistive switching behaviors and mechanisms in an annealed Ni/ZrO₂/TaN memory device, *Journal of Physics D: Applied Physics*, Volume 48, Issue 3, 28 January 2015, Article number 035108. <https://doi.org/10.1088/0022-3727/48/3/035108>
- [54] Chen Q., Yang W., Zhu J., Fu L., Li D., Zhou L. In situ fluorine doped ZrO_{2-x} nanotubes for efficient visible light photocatalytic activity // *Journal of Materials Science: Materials in Electronics*, Volume 30, Issue 1, 15 January 2019, Pages 701-710. <https://doi.org/10.1007/s10854-018-0339-8>
- [55] Yang D., Wang Y.-Q., Ren G.-B., Feng S., Chen Y.-Y., Wang W.-Z. Formation mechanism study of TiO₂ film comprising nanotubes and nanoparticles // *Chinese Journal of Chemical Physics*, Volume 25, Issue 1, February 2012, Article number 013, Pages 91-95. <https://doi.org/10.1088/1674-0068/25/01/91-95>
- [56] Hamidreza Arab Bafrani, Mahdi Ebrahimi, Saeed Bagheri Shouraki, Alireza Z. Moshfegh A facile approach for reducing the working voltage of Au/TiO₂/Au nanostructured memristor by enhancing the local electric field // *Nanotechnology* 29 (2018) 015205 <https://doi.org/10.1088/1361-6528/aa99b7>
- [57] Yuan Y., Cao X., Sun Y., Su J., Liu C., Cheng L., Li Y., Yuan L., Zhang H., Li J. Intrinsic mechanism in nonvolatile polycrystalline zirconium oxide sandwiched structure // *Journal of Materials Science: Materials in Electronics*, Volume 29, Issue 3, 1 February 2018, Pages 2301-2306. <https://doi.org/10.1007/s10854-017-8146-1>
- [58] Lampert M.A., Mark P. *Current Injection in Solids*. Academic Press, New York, 1970, 354 pp.
- [59] Chiu F.-C. A Review on Conduction Mechanisms in Dielectric Films // *Advances in Materials Science and Engineering*, Volume 2014, Article ID 578168, 18 pages. <http://dx.doi.org/10.1155/2014/578168>
- [60] Lim E.W., Ismail R. Conduction mechanism of valence change resistive switching memory: A survey // *Electronics (Switzerland)*, Volume 4, Issue 3, 9 September 2015, Pages 586-613. <https://doi.org/10.3390/electronics4030586>
- [61] Lin C.Y., Wang S.Y., Lee D.Y., Tseng T.Y. Electrical Properties and Fatigue Behaviors of ZrO₂ Resistive Switching Thin Films // *Journal of Electrochemical Society*, Volume 155, Issue 8, 2008, Pages H615-H619. <https://doi.org/10.1149/1.2946430>
- [62] Pimenov A., Ullrich J., Lunkenheimer P., Loidl A., Rüscher C.H. Ionic conductivity and relaxations in ZrO₂-Y₂O₃ solid solutions // *Solid State Ionics*, Volume 109, Issues 1-2, 1 June 1998, Pages 111-118. [https://doi.org/10.1016/S0167-2738\(98\)00082-4](https://doi.org/10.1016/S0167-2738(98)00082-4)

-
- [63] Llewelyn Leach J.S., Pearson B.R. The effect of foreign ions upon the electrical characteristics of anodic ZrO₂ films // *Electrochimica Acta*, Volume 29, Issue 9, September 1984, Pages 1271-1282. [https://doi.org/10.1016/0013-4686\(84\)87190-X](https://doi.org/10.1016/0013-4686(84)87190-X)
- [64] Weppner W. Electronic transport properties and electrically induced p-n junction in ZrO₂ + 10 m/o Y₂O₃ // *Journal of Solid State Chemistry*, Volume 20, Issue 3, March 1977, Pages 305-314. [https://doi.org/10.1016/0022-4596\(77\)90167-0](https://doi.org/10.1016/0022-4596(77)90167-0)
- [65] Sasaki K., Maier J. Re-analysis of defect equilibria and transport parameters in Y₂O₃-stabilized ZrO₂ using EPR and optical relaxation // *Solid State Ionics*, Volume 134, Issue 3-4, 2 October 2000, Pages 303-321. [https://doi.org/10.1016/S0167-2738\(00\)00766-9](https://doi.org/10.1016/S0167-2738(00)00766-9)
- [66] Chen C.-C., Say W.C., Hsieh S.-J., Diao E.W.-G. A mechanism for the formation of annealed compact oxide layers at the interface between anodic titania nanotube arrays and Ti foil // *Applied Physics A: Materials Science and Processing*, Volume 95, Issue 3, June 2009, Pages 889-898. <https://doi.org/10.1007/s00339-009-5093-6>
- [67] Roh B., Macdonald D.D. Effect of oxygen vacancies in anodic titanium oxide films on the kinetics of the oxygen electrodereduction // *Russian Journal of Electrochemistry* Volume 43, Issue 2, February 2007, Pages 125-135. <https://doi.org/10.1134/S1023193507020012>
- [68] Sang L.X., Zhang Z.Y., Ma C.F. Photoelectrical and charge transfer properties of hydrogen-evolving TiO₂ nanotube arrays electrodes annealed in different gases // *International Journal of Hydrogen Energy*, Volume 36, Issue 8, April 2011, Pages 4732-4738. <https://doi.org/10.1016/j.ijhydene.2011.01.071>
- [69] Hanzu I., Djenizian T., Knauth P. Electrical and point defect properties of TiO₂ nanotubes fabricated by electrochemical anodization // *Journal of Physical Chemistry C*, Volume 115, Issue 13, 7 April 2011, Pages 5989-5996. <https://doi.org/10.1021/jp1111982>
- [70] Tse K., Robertson J. Defect passivation in HfO₂ gate oxide by fluorine // *Applied Physics Letters*. Volume 89, Issue 14, 2006, Article number 142914. <https://doi.org/10.1063/1.2360190>
- [71]. Xue W., Gao S., Shang J., Yi X., Liu G., Li R.-W. Recent Advances of Quantum Conductance in Memristors // *Advanced Electronic Materials*. Volume 5, Issue 9, 1 September 2019, Article number 1800854. <https://doi.org/10.1002/aelm.201800854>
- [72] Grado-Caffaro M.A., Grado-Caffaro M. Theoretical evaluation of electron mobility in multi-walled carbon nanotubes // *Optik*, Volume 115, Issue 1, 2004, Pages 45-46. <https://doi.org/10.1078/0030-4026-00326>
- [73] Fu-Chien Chiu, Zhi-Hong Lin, Che-Wei Chang, Chen-Chih Wang, Kun-Fu Chuang, Chih-Yao Huang, Joseph Ya-Min Lee, and Huey-Liang Hwang "Electron conduction mechanism and band diagram of sputter-deposited Al/ZrO₂/Si structure", *Journal of Applied Physics* 97, 034506 (2005). <https://doi.org/10.1063/1.1846131>
- [74] Muratore F., Baron-Wiechéc A., Hashimoto T., Gholinia A., Skeldon P., Thompson G.E. Growth of nanotubes on zirconium in glycerol/fluoride electrolytes // *Electrochimica Acta*, Volume 56, Issue 28, 1 December 2011, Pages 10500-10506. <https://doi.org/10.1016/j.electacta.2010.12.089>
- [75] Wu Y., Chen J., Hu W., Zhao K., Qu P., Shen P., Zhao M., Zhong L., Chen Y. Phase transformation and oxygen vacancies in Pd/ZrO₂ for complete methane oxidation under lean conditions // *Journal of Catalysis*, Volume 377, September 2019, Pages 565-576. <https://doi.org/10.1016/j.jcat.2019.04.047>
- [76] Habazaki H., Fushimi K., Shimizu K., Skeldon P., Thompson G.E. Fast migration of fluoride ions in growing anodic titanium oxide // *Electrochemistry Communications*, Volume 9, Issue 5, May 2007, Pages 1222-1227. <https://doi.org/10.1016/j.elecom.2006.12.023>

-
- [77] Shimizu K., Kobayashi K., Thompson G.E., Skeldon P., Wood G.C. The migration of fluoride ions in growing anodic oxide films on tantalum // *Journal of the Electrochemical Society*, Volume 144, Issue 2, February 1997, Pages 418-423. <https://doi.org/10.1149/1.1837425>
- [78] Carta D., Salaoru I., Khat A., Regoutz A., Mitterbauer C., Harrison N.M., Prodromakis T. Investigation of the Switching Mechanism in TiO₂-Based RRAM: A Two-Dimensional EDX Approach // *ACS Applied Materials and Interfaces*, Volume 8, Issue 30, 3 August 2016, Pages 19605-19611. <https://doi.org/10.1021/acsami.6b04919>